

# Free-breathing & ungated cardiac MRI using iterative SToRM (i-SToRM)

Yasir Q Mohsin, Sunrita Poddar, and Mathews Jacob

**Abstract**—We introduce a local manifold regularization approach to recover dynamic MRI data from highly undersampled measurements. The proposed scheme relies on the manifold structure of local image patches at the same spatial location in a free-breathing cardiac MRI dataset; this approach is a generalization of the SToRM (Smoothness Regularization on Manifolds) scheme that exploits the global manifold structure of images in the dataset. Since the manifold structure of the patches varies depending on the spatial location and is often considerably simpler than the global one, this approach significantly reduces the data demand, facilitating the recovery from shorter scans. Since the navigator-based estimation of manifold structure pursued in SToRM is not feasible in this setting, a reformulation of SToRM is introduced. Specifically, the regularization term of the cost function involves the sum of robust distances between images sub-patches in the dataset. The optimization algorithm alternates between updating the images and estimating the manifold structure of the image patches. The utility of the proposed scheme is demonstrated in the context of *in-vivo* prospective free-breathing cardiac CINE MRI imaging with multichannel acquisitions as well as simulated phantoms. The new framework facilitates a reduction in scan time, as compared to the SToRM strategy.

## I. INTRODUCTION

THE slow nature of MRI acquisitions poses several challenges in dynamic imaging applications such as cardiac MRI, due to the need for high spatial and temporal resolution. The standard practice in cardiovascular MRI is to collect k-t space data in a breath-held and segmented mode. Specifically, respiration is suspended during data acquisition and the k-space data from multiple cardiac cycles are merged together to form the images. This approach often makes it challenging to acquire data from several patient groups (e.g. claustrophobic, pediatric subjects and obese patients), who have difficulty in holding their breath. In addition, the achievable spatial resolution is often severely limited by the typical breath-hold durations. Another challenge is the long duration of the exam, which makes cardiac MRI expensive and reduces patient comfort.

Respiratory gating methods were introduced to eliminate the need for breath-holding. These methods rely on respiratory bellows, self-gating, or navigator signals [1], [2] to select the k-space data from a specific respiratory phase. The main challenge associated with these methods is the low acquisition efficiency. While low-rank methods [3]–[6] provide good reconstructions in breath-held mode, the direct application of these methods to the setting with extensive cardiac and

respiratory motion is challenging. Motion-compensated reconstruction schemes were introduced to improve acquisition efficiency [7]–[11]. These approaches rely on joint compressed sensing and motion compensation to recover the images from multiple phases simultaneously, while estimating the motion between phases using deformable registration. The main downside of these schemes is the considerable computational complexity needed to recover the data from multiple cardiac and respiratory phases. Recently, several researchers have proposed motion-resolved recovery schemes, which estimate the cardiac and respiratory phases from golden angle radial acquisitions. These methods estimate the phase information by filtering the series of central k-space samples acquired at each shot [12], [13]. The binned four dimensional data (two spatial dimensions, a respiratory dimension, and a cardiac phase dimension) is then recovered using spatiotemporal total variation regularization. While the good performance of these methods have been demonstrated in several subjects, their utility in subjects with irregular respiration and cardiac motion (e.g. arrhythmia) is not clear. The use of navigators at every alternate acquisition considerably simplifies the estimation of the phases as shown in [5], [13]. However, this approach comes at the expense of 50% overhead in acquiring the navigator signal.

In this work, we will build upon our recent SToRM framework [14] and related manifold-based approaches [15], which rely on an implicit binning strategy using navigators. SToRM assumes the images in a free-breathing and ungated dataset to be points on a smooth and low-dimensional manifold. The Laplacian matrix that specifies the structure of the manifold, or equivalently the similarity between image pairs in the dataset, is estimated from navigator signals. The main advantage of this implicit motion-resolved scheme over explicit binning strategies is the recovery of the natural dynamics in a real-time acquisition mode. While this approach offers good reconstructions, SToRM’s dependency on radial navigators lowers the scanning acquisition efficiency. Specifically, 2-4 radial lines per frame are usually needed for good recovery and approximately 20-40% of the scan time is devoted to the acquisition of those navigators. This approach also results in reduced incoherence between sampling patterns of different frames, and makes it difficult for the future extension of this scheme to 3-D applications. Another challenge is that SToRM requires a relatively long acquisition duration ( $\approx 1$  minute per slice) to ensure that the complex image manifold is well-sampled. Specifically, since SToRM relies on the similarity between images in the dataset, a large number of time series are needed to ensure that all the phases are well represented.

The focus of this work is to overcome the drawbacks associated with SToRM while maintaining the good quality of the recon, by exploiting the manifold structure of localized image patches in the dataset. Note that the individual regions of the images experience very different motion patterns. For example, the manifold structure of patches within the heart, which experience both cardiac and respiratory motion, are significantly different from those in the lung regions that experience only respiratory motion, or static regions. Separately exploiting the manifold structure of these localized regions is far more effective; since the manifolds are relatively simpler, fewer images (and hence shorter acquisitions) are sufficient to ensure good sampling. We thus expect the local manifold regularization to be far more effective than the global approach pursued in SToRM. The direct extension of SToRM to this setting is difficult since the navigators only provide global manifold structure and not the local one. We hence introduce a generalization of the SToRM framework, which eliminates the need for navigators. Specifically, the image recovery is formulated as a regularized optimization problem, where the regularization term involves the sum of robust distances between images in the dynamic dataset. Inspired by our past work [16]–[18], we use saturating distance functions that are insensitive to large image differences. By contrast, we compare each patch with all the patches at the same spatial location, facilitating implicit motion-resolved reconstruction. We use a majorize minimize algorithm to solve the above non-convex optimization problem. This algorithm alternates between the following two steps (i) the estimation of a graph Laplacian matrix from the current image sub-patches estimate, and (ii) the estimation of the image sub-patches using the graph Laplacian matrix. Since each step of the proposed algorithm is similar to SToRM, we term the new approach as iterative SToRM (i-SToRM). We use homotopy continuation strategies to encourage the convergence of the algorithm to the global minimum of the cost function. The SToRM scheme can be interpreted as the first iteration of an algorithm to minimize the above criterion, where the manifold Laplacian matrix is obtained without the use of navigators. In addition to eliminating the dependence on navigators, this approach facilitates the extension of the global SToRM framework to exploit the local manifold structure of image patches.

The main difference of the proposed scheme with our recent patch-based PRICE formulation [17] is the choice of the patch neighborhood used for comparison. PRICE achieves implicit motion compensation by exploiting the similarity of rectangular sub-patches in a frame with other patches in its spatiotemporal neighborhood. By contrast, the proposed formulation achieves implicit motion-resolved reconstruction by harnessing the non-local similarities of patches with other patches in the dataset. While this approach may be combined with PRICE to additionally achieve motion compensation, the direct application of our PRICE scheme to large datasets in the current application is computationally challenging due to the large number of patch pairs that are involved in the comparison. In contrast, iSToRM considers larger patches and reduces the number of patch pairs involved in the comparison, thus keeping the computational complexity manageable.

We determine the utility of the proposed scheme in the context of recovering numerical phantoms as well as *in-vivo* prospective cardiac CINE MRI datasets with multichannel acquisitions. The prospective datasets are challenging cases since they are acquired in the ungated mode, accelerated by a high undersampling factor and a considerable cardio-respiratory motion is present due to the free-breathing scan.

## II. METHODS

### A. Acquisition scheme

The multicoil undersampled acquisition of the dynamic MRI dataset  $\mathbf{f}(x, y, t) : \mathbb{Z}^3 \rightarrow \mathbb{C}$  can be modeled as:

$$\mathbf{b}_i(\mathbf{k}, t) = \int_{\mathbf{r}} f(\mathbf{r}, t) s_i(\mathbf{r}) e^{j(\mathbf{k}^T \mathbf{r})} d\mathbf{r} + \mathbf{n}(\mathbf{r}, t) \quad (1)$$

Here,  $\mathbf{r} = (x, y)$  and  $\mathbf{k} = (k_x, k_y)$  denote the spatial variable and k-space location, respectively.  $\mathbf{b}(\mathbf{k}, t)$  represents the k-space measurements from all the coils, while  $f(\mathbf{r}, t)$  is the dynamic dataset, and  $s_i(\mathbf{r})$  denotes the  $i^{\text{th}}$  coil sensitivity pattern. We assume  $\mathbf{n}$  to be complex zero mean Gaussian distributed white noise of a specified standard deviation  $\sigma$ . The above relations can be compactly expressed in the vector form as:

$$\mathbf{B} = \mathcal{A}(\mathbf{F}) + \mathbf{N}, \quad (2)$$

where  $\mathcal{A}$  is the multi-channel undersampling forward model. Here  $\mathbf{F}$  is the Casorati matrix of the dynamic dataset  $f(\mathbf{r}, t)$ .

### B. SToRM reconstruction

The SToRM recovery of the dynamic MRI dataset  $\mathbf{F}$  from its undersampled Fourier measurements  $\mathbf{B}$  is posed as [14]:

$$\mathbf{F}^* = \arg \min_{\mathbf{F}} \|\mathcal{A}(\mathbf{F}) - \mathbf{B}\|_2^2 + \lambda \sum_{i=1}^N \sum_{j=1}^N w_{i,j} \|\mathbf{f}_i - \mathbf{f}_j\|^2 \quad (3)$$

where  $\mathbf{f}_i$  is the  $i^{\text{th}}$  frame in the dynamic dataset, and hence is the  $i^{\text{th}}$  column of the Casorati matrix  $\mathbf{F}$  and  $N$  is the total number of frames in the time series. A navigated acquisition strategy was used to estimate the matrix  $\mathbf{W}$  with entries  $w_{i,j}$ , which captures the manifold structure. The measurement operator at the  $i^{\text{th}}$  frame is chosen as:

$$\mathbf{b}_i = \underbrace{\begin{bmatrix} \Phi \\ \mathbf{B}_i \end{bmatrix}}_{\mathbf{A}_i} \mathbf{f}_i \quad (4)$$

Here,  $\mathbf{A}_i$  is multichannel sampling operator for the  $i^{\text{th}}$  frame. It is the concatenation of the navigator sampling operator  $\Phi$ , which is fixed across all frames, and  $\mathbf{B}_i$  which varies from frame to frame. The structure of the manifold specified by the weights  $w_{i,j}$ , are estimated from navigators as below:

$$w_{i,j} = \exp - \frac{\|\Phi \mathbf{x}_i - \Phi \mathbf{x}_j\|^2}{\sigma^2} \quad (5)$$

It was shown that (3) can also be expressed as:

$$\mathbf{F}^* = \arg \min_{\mathbf{F}} \|\mathcal{A}(\mathbf{F}) - \mathbf{B}\|_2^2 + \lambda \text{trace}(\mathbf{F} \mathbf{L} \mathbf{F}^H), \quad (6)$$

where:

$$\mathbf{L} = \mathbf{D} - \mathbf{W} \quad (7)$$

and  $\mathbf{D}$  is a diagonal matrix with entries  $d_{i,i} = \sum_j w_{i,j}$ .  $\mathbf{L}$  is often termed as the graph Laplacian operator, which can be viewed as the discrete approximation of the Laplace Beltrami operator on the manifold. The trace of a square matrix is defined as the sum of the elements on the main diagonal, and  $\mathbf{F}^H$  denotes the conjugate transpose of  $\mathbf{F}$ .

### C. Calibration-free *i*-SToRM

We formulate the reconstruction of the images from their highly undersampled measurements as the following unconstrained optimization problem:

$$\mathbf{F}^* = \arg \min_{\mathbf{F}} \|\mathcal{A}(\mathbf{F}) - \mathbf{B}\|_2^2 + \lambda \underbrace{\sum_{i=1}^N \sum_{j=1}^N \varphi(\|\mathbf{f}_i - \mathbf{f}_j\|)}_{\mathcal{C}} \quad (8)$$

The regularization penalty  $\mathcal{C}$  involves the sum of unweighted robust distances between images in the dataset. This is in contrast to (3) that uses weighted quadratic distances between frames, which requires the knowledge of the manifold or equivalently the weights  $w_{i,j}$ . We choose the regularization prior  $\varphi$  as a saturating distance metric that penalizes small distances heavily, while it saturates with large distances. In this work, we use the  $H_1$  metric [16], specified by:

$$\varphi(t) = 1 - \exp(-t^2/2\sigma^2) \quad (9)$$

The Taylor series expansion of  $\varphi(t)$  shows that  $\varphi(t) \approx \frac{t^2}{\sigma^2} + \mathcal{O}(t^4)$ , which implies that  $\varphi$  can be safely assumed to be a quadratic/Euclidean distance metric for small values of  $t$ . Note that the geodesic distances (distances on the manifold) between neighboring points on the manifold can be safely approximated by their Euclidean distances. By contrast, Euclidean distances between points that are distant on the manifold are not good approximations for the geodesic distance. The use of the saturating prior eliminates such terms from the cost function. In particular, pairs of frames that have a large inter-frame Euclidean distance do not contribute to the gradient of the cost function, even though they amount to constant terms in the regularization prior. The proposed scheme exploits the non-local redundancy between frames that may be well separated in time. In particular, (8) facilitates the implicit sharing of data between similar frames. This implicit approach can be seen as an alternative to explicitly binning the dynamic data from different respiratory and cardiac phases, followed by the recovery of the bins [12]. Since the regularization term is non-convex, we use homotopy continuation strategies to encourage the convergence of the algorithm to the global minimum. While this approach is not guaranteed to converge to a global minimum, it is widely used in non-convex compressive sensing and usually results in good solutions [19].

### D. Relationship to SToRM

Inspired by [16], we use a majorize minimize algorithm to solve (8). This majorization strategy has been introduced in [20] and has been widely used in convex and non-convex

image recovery with iterative reweighted algorithms. The non-convex prior (second term in (8)) can be majorized as the sum of quadratic distances between images in the dynamic dataset:

$$\varphi(\|\mathbf{f}_i - \mathbf{f}_j\|) \leq w_{i,j} \|\mathbf{f}_i - \mathbf{f}_j\|^2 \quad (10)$$

where the new inter-frame weights are specified by  $w_{i,j} = \psi(\|\mathbf{f}_i - \mathbf{f}_j\|)$ . Here,

$$\psi(t) = \begin{cases} \exp\left(-\frac{t^2}{2\sigma^2}\right) & \text{if } t^2 < T \\ 0 & \text{else.} \end{cases} \quad (11)$$

Note that the function  $\psi(0) = 1$ , while it decays with increasing value of  $t$ . The use of the majorization in (10) ensures that similar images are averaged together, while dissimilar images are excluded from the averaging process. This majorization provides a two-step approach, which alternates between the estimation of the weights from the current images using (11) and solving for the images using (8). Thus, this approach can be viewed as an iterative version of SToRM, where the weights are estimated from the current image iterate rather than the  $k$ -space navigators as in (5).

While more efficient optimization strategies such as alternating direction method of multipliers do exist, the use of these methods along with non-convex priors may suffer from local minima issues. By contrast, the monotonic convergence offered by the majorize minimize framework, along with efficient continuation strategies, can be combined to encourage the convergence of the algorithm to the global minimum of (8).

### E. *i*-STORM with patches

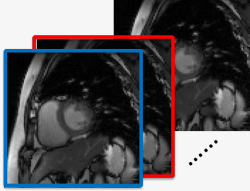
The formulation in (8) facilitates the exploitation of the manifold structure of images in the dataset without explicit navigators. We note that different spatial regions in the dataset will experience different types of motion. For example, the cardiac regions are expected to experience cardiac and respiratory motion, while the lung regions far away from the heart are expected to be independent of cardiac motion. To exploit the spatial variation in manifold structure, we generalize (8) to account for the manifold structure of image sub-patches. Specifically, we formulate the recovery as:

$$\mathbf{F}^* = \arg \min_{\mathbf{F}} \|\mathcal{A}(\mathbf{F}) - \mathbf{B}\|_2^2 + \lambda \sum_{\mathbf{r}_k} \underbrace{\sum_{i=1}^{N_f} \sum_{j=1}^{N_f} \varphi(\|\mathcal{P}_{\mathbf{r}_k}(\mathbf{f}_i - \mathbf{f}_j)\|)}_{\mathcal{C}_{\mathbf{r}_k}} \quad (12)$$

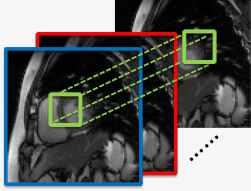
Here,  $\mathcal{P}_{\mathbf{r}}(\mathbf{f})$  is a patch extraction operator, which extracts a square shaped 2-D image patch centered at the spatial location  $\mathbf{r}$  from the dynamic dataset  $\mathbf{f}$ :

$$\mathcal{P}_{\mathbf{r}}(\mathbf{f}) = f(\mathbf{r} + \mathbf{p}), \mathbf{p} \in \mathcal{K} \quad (13)$$

Here,  $\mathcal{K}$  denotes the square shape neighborhood of size of dimension  $(N+1) \times (N+1)$ , centered at  $\mathbf{r}$ . The set of spatial locations  $\mathbf{r}_k$ , or equivalently the patches, are chosen to span the entire image. For example, the set can be chosen as a set of overlapping or non-overlapping patches. Note that the penalty term  $\mathcal{C}(\mathbf{r}_k)$  is essentially the same as the

$$\mathbf{F}^* = \arg \min_{\mathbf{F}} \|\mathcal{A}(\mathbf{F}) - \mathbf{B}\|_2^2 + \lambda \sum_{i=1}^{N_f} \sum_{j=1}^{N_f} w_{i,j} \|\mathbf{f}_i - \mathbf{f}_j\|^2$$


**(a) SToRM**

$$\mathbf{F}^* = \arg \min_{\mathbf{F}} \|\mathcal{A}(\mathbf{F}) - \mathbf{B}\|_2^2 + \lambda \sum_{\mathbf{r}_k} \sum_{i=1}^{N_f} \sum_{j=1}^{N_f} \varphi(\|\mathcal{P}_{\mathbf{r}_k}(\mathbf{f}_i - \mathbf{f}_j)\|)$$


**(b) i-SToRM**

Fig. 1: Illustration of the proposed i-SToRM scheme (b), in comparison with the SToRM scheme in (a). The regularization term in SToRM involves the sum of weighted  $\ell_2$  distances between images in the dataset, where the weights are estimated from navigators. By contrast, the regularization scheme in i-SToRM is the sum of unweighted robust distances between image sub-patches in the dataset. Specifically, the patches of size  $N \times N$  indicated by the green neighborhood are compared with each other using the distance metric, which saturates with large distances. The center of the patches, specified by  $\mathbf{r}_k$  are chosen to span the entire image with a specified stride; the patches are overlapping in space to reduce blocky artifacts in the image and suppress noise. The main difference between these formulations is the distance metric. We use an alternating minimization to solve for the i-SToRM scheme, which alternates between the estimation of the manifold Laplacian and the images; this approach eliminates the need for the use of navigators and allows the extension of the SToRM scheme to exploit the manifold structure of local patches. When the size of the patches is the same as the size of the images, the first iteration of the i-SToRM scheme is equivalent to the SToRM setting.

penalty term  $\mathcal{C}$  in (8), restricted the smaller set of images  $\mathcal{P}_{\mathbf{r}_k}(f_i); i = 1, \dots, N$ . See Figure 1, where the comparisons are restricted to a cube, centered at the spatial location  $\mathbf{r}_k$ . The motion parameters within different spatial regions/cubes are expected to be very different in cardiac MRI. This restriction results in a considerably simpler manifold in regions with no motion or regions with only respiratory motion, which is essentially most of the field of view (FOV). Thus, the generalization is expected to be a more adaptive version of SToRM. Note that (8) is a special case of (12), when the size of the patch is the same size of each image, and only one  $\mathbf{r}_k$  is considered.

We observe that the SToRM approach of calibration-based estimation of the manifold structure is not feasible in the patch-based setting. Specifically, k-space navigators only provide global information about the whole FOV, which can only be used to estimate the image manifold structure. The localized manifold structure estimation is facilitated by the reformulation of (8).

#### F. Two step iterative algorithm using MM

We use the majorize minimize (MM) framework to solve for (12). The non-convex patch-based prior (second term in (12)) can be majorized as the sum of quadratic distances between image sub-patches in the dynamic dataset:

$$\varphi(\|\mathcal{P}_{\mathbf{r}_k}(\mathbf{f}_i - \mathbf{f}_j)\|) \leq w_{i,j,\mathbf{r}_k} \|\mathcal{P}_{\mathbf{r}_k}(\mathbf{f}_i - \mathbf{f}_j)\|^2 \quad (14)$$

where the new inter-frame weights can be self-estimated from the undersampled dataset, as opposed to the navigators used in SToRM.

Using the majorization in (12), we obtain an alternating minimization strategy, which alternates between updating the

images and the weights/Laplacian operators.

**Images update:** Once the weights are available, the images can be estimated as:

$$\mathbf{F}^* = \arg \min_{\mathbf{F}} \|\mathcal{A}(\mathbf{F}) - \mathbf{B}\|_2^2 + \lambda \sum_{\mathbf{r}_k} \text{trace}(\mathbf{F}_k \mathbf{L}_k \mathbf{F}_k^H) \quad (15)$$

where  $\mathbf{F}_k$  is the Casorati matrix:

$$\mathbf{F}_k = [\mathcal{P}_{\mathbf{r}_k}(f_1), \dots, \mathcal{P}_{\mathbf{r}_k}(f_{N_f})] \quad (16)$$

of the patch time series  $\mathcal{P}_{\mathbf{r}_k}(f_i), i = 1, \dots, N_f$ . We can think of  $\mathbf{F}_k = \mathcal{Q}_k(\mathbf{F})$ , where  $\mathcal{Q}_k$  is an operator that extracts the cube of data centered at the spatial location  $\mathbf{r}_k$  and constructs a Casorati matrix out of it. The matrices  $\mathbf{L}_k = \mathbf{D}_k - \mathbf{W}_k$  are the Laplacians of the patch time series  $\mathbf{F}_k$ . We observe that (15) is the extension of (6) to the patch setting.

The Euler-Lagrange equation for the above quadratic equation is given by:

$$\mathcal{A}^* \mathcal{A}(\mathbf{F}) + 2 \lambda \sum_{\mathbf{r}_k} \mathcal{Q}_k^* \left( \underbrace{\mathcal{Q}_k(\mathbf{F})}_{\mathbf{F}_k} \mathbf{L}_k \right) = \mathcal{A}^* \mathbf{B} \quad (17)$$

Here,  $\mathcal{A}^*$  denotes the adjoint of the operator  $\mathcal{A}$ . The second term on the l.h.s involves the extraction of the Casorati matrix  $\mathbf{F}$ , multiplication by  $\mathbf{L}_k$ , followed by putting the entries of the Casorati matrix back at the appropriate location. The optimization problem (17) can be efficiently solved using conjugate gradients.

**Weights update:** The Laplacian matrices, or equivalently the weights, are estimated from the current image series  $\mathbf{F}$  as:

$$(\mathbf{W}_k)_{i,j} = \psi(\|\mathcal{P}_{\mathbf{r}_k}(\mathbf{f}_i - \mathbf{f}_j)\|) \quad (18)$$

where  $\psi$  is specified by (11). Note that the inter-patch distance

metric in (9) was chosen to heavily penalize small differences between the patches, while the metric saturates for large sub-patch differences. In STORM, the weight matrix was sparsified to retain only a fixed number (e.g. three in [14]) of nearest neighbors for each frame, irrespective of the magnitude of the inter-frame differences. By contrast, we rely on (11) to compute the weights; the weights are set to zero, when the inter-frame differences fall above a specified threshold. Note that this approach provides a variable number of neighbors for each frame, depending on the magnitude of the inter-patch differences; and that is consistent with the saturating function  $\varphi$  that we assumed in this work.

**Algorithm II.1:** 1-STORM( $\mathcal{A}, \mathbf{B}$ )

**Input :**  $\mathbf{B} =$  k-space measurements  
 $\mathbf{F}_{\text{init}} = \mathbf{B};$   
**while**  $i < \#$  Outer Iterations  
  **do**  $\left\{ \begin{array}{l} \text{Update } \mathbf{F} \text{ by solving (17) using CG;} \\ \text{Update weight matrices } \mathbf{W}_k \text{ using (18);} \\ \text{Derive the Laplacians } \mathbf{L}_k \text{ from } \mathbf{W}_k \text{ using (7);} \end{array} \right.$   
**return** ( $\mathbf{F}$ )

*G. Datasets and sampling pattern*

We validate the proposed algorithm using a numerical phantom, which mimics the motion resulting from time-varying heart rates and respiratory motion [21]. The data was generated by warping a ground truth breath-held dataset using realistic synthetic respiratory motion fields and stretching of the cardiac cycle. This free breathing dataset has a reasonable amount of inter-frame motion due to respiratory dynamics. The dataset has 200 phase encodings, 256 samples per readout and 256 temporal frames.

We also validate the proposed algorithm using experiments on two *in-vivo* free-breathing and ungated cardiac CINE datasets with radial undersampling settings. They were acquired using protocols approved by the Institutional Review Board (IRB) at the University of Iowa. The prospectively undersampled MR imaging was acquired using radial FLASH sequence on a Siemens Skyra 3T scanner with 24 coil elements total (body and spine coil arrays). The datasets were acquired from congenital heart patients, who were instructed to breathe freely in all of the studies. The images were acquired in short axis and 4-chamber view to test the sensitivity of the algorithm to geometry. The short axis data was acquired using the calibration-based scheme in [14] as well as a golden angle acquisition scheme. By using the equiangular spacing within each frame, we ensure that the entire k-space is covered uniformly.

The sequence parameters were: TR/TE 4.68/2.1 ms, FOV 300mm, base resolution 256, slice thickness = 5 mm, phase encodes  $\times$  frequency encodes: 512  $\times$  512. A temporal resolution of 46.8 ms was achieved by sampling 10 lines of k-space per frame. 1000 radial lines of k-space were acquired per slice which resulted in an acquisition time of around 46.8 s. The acquisition using 10 rays corresponds to an acceleration factor of  $\approx 25.6$  fold when compared to Nyquist. The scan

parameters were kept the same across all views for the entire prospective datasets.

*H. Metrics used for quantitative comparison*

The retrospective reconstructions were quantitatively compared to the reference data using the following metrics. We evaluated these metrics on the whole time series on both global FOV and a square region of interest containing the heart.

- Signal to Error Ratio (SER):

$$\text{SER} = 20 \log_{10} \left( \frac{\|\mathbf{\Gamma}_{\text{orig}}\|_2}{\|\mathbf{\Gamma}_{\text{orig}} - \mathbf{\Gamma}_{\text{rec}}\|_2} \right),$$

where  $\|\cdot\|_2$  denotes the  $\ell_2$  norm, and  $\mathbf{\Gamma}_{\text{orig}}, \mathbf{\Gamma}_{\text{rec}}$  denote the original and the reconstructed images respectively.

- Normalized High Frequency Error (HFEN) [22]: It measures the quality of fine features, edges, and spatial blurring in the images and defined as:

$$\text{HFEN} = 20 \log_{10} \left( \frac{\|\text{LoG}(\mathbf{\Gamma}_{\text{orig}})\|_2}{\|\text{LoG}(\mathbf{\Gamma}_{\text{orig}}) - \text{LoG}(\mathbf{\Gamma}_{\text{rec}})\|_2} \right),$$

where LoG is a Laplacian of Gaussian filter that captures edges. We use the same filter specifications as [22]; kernel size of 15  $\times$  15 pixels, with a standard deviation of 1.5.

- The Structural SIMilarity index (SSIM) is a perceptual metric introduced in [23]. We used the toolbox introduced by [23], with default contrast values [0.01 0.03], Gaussian kernel size of 11  $\times$  11 pixels with a standard deviation of 1.5 pixels.
- Global phase coherence (GPC) index [24] provides a measure of image sharpness by estimating the volume of all possible phase functions associated with the measured modulus, which produces images that are not less likely than the original image. The likelihood is measured with the total variation implicit prior, and is numerically evaluated using a Monte-Carlo simulation. We used the toolbox introduced by Blanchet et al [24] to evaluate the index.

*I. Implementation*

The algorithms were implemented using a single node of a high-performance Argon Cluster at the University of Iowa, equipped with Intel Xeon CPU with 28 Cores at 2.40GHz with 128 GB of memory running on Red Hat Linux MATLAB R2016b. The prospective datasets were acquired using 10,000 radial spokes, which corresponded to an acquisition time of around 50 seconds per slice.

We binned the data to 10 spokes/frame, which translates to 1000 frames. Our earlier STORM scheme required 1000 frames to obtain good reconstructions. By contrast, we only rely on the first 300 time frames in this work for reconstruction. The proposed scheme considers joint recovery of the dataset with a large number of frames and several receiver coils from their non-Cartesian Fourier samples. The direct implementation of this scheme using NUFFT and keeping the entire channels requires large memory demand and high computational complexity. We rely on few simplifications to realize a fast and

memory efficient algorithm, parts of which can be sped up using GPU acceleration.

Pre-interpolation to a Cartesian grid: The radially acquired datasets were first pre-interpolated into a Cartesian grid, which allows us to implement the conjugate gradients algorithm using fast Fourier transform (FFT) rather than non-uniform fast Fourier transform (NUFFT). Specifically, the forward model corresponds to FFT of the sensitivity weighted images, multiplied by density weighted sampling masks. We, and our collaborators, have compared the accuracy of this pre-interpolation strategy in our previous studies (e.g. kt-SLR, [3]). To further confirm this finding, we have performed a comparison of the STORM reconstructions with NUFFT and using the pre-interpolation strategy on a smaller dataset. To further confirm this finding, we have performed a comparison of the STORM reconstructions with NUFFT and using the pre-interpolation strategy on a smaller dataset. The experiment, shown in the last slide of the supplementary material, shows that the differences between the NUFFT-based evaluation and the above pre-interpolation strategy are minor for radial trajectories. We note that the pre-interpolation is equivalent to  $\mathcal{A}^* \mathbf{B}$ . It is shown that  $(\mathcal{A}^* \mathcal{A})$  has a Toeplitz structure that can be implemented as a multiplication in the Fourier domain by a  $2N \times 2N$  matrix. Thus, accounting for the density and interpolation weights into the sampling masks (using  $N \times N$  FFT) is equivalent to performing a circulant approximation of the above operation. We believe that the circulant approximation is accurate for radial trajectories, but not valid in general. In the interest of realizing a fast algorithm, we utilize the pre-interpolation strategy for the rest of the experiments.

Coil compression: The datasets were acquired with 24 coils, out of which many had low sensitivities in the region/slice of interest, resulting in noisy measurements. We used an automatic algorithm to pre-select the best 10 coil images; we observed that removing the un-reliable coils resulted in improved reconstructions. This algorithm binned the k-space data from several images to recover the low-resolution coil images. We then used the PCA coil combination using SVD such that the approximation error is  $< 5\%$ . In most cases, we note that 5-6 coils were sufficient to bring the approximation error to  $< 5\%$ . The coil sensitivity maps were estimated from these coil combined virtual channels using the method designed by Walsh et al [25] and assumed to be constant over time. Our experiments (not included in the paper) show that this coil combination has minimal impact on image quality. The main motivation for the combination was to reduce the footprint of the algorithm to fit it on our GPU device, which significantly reduced the computational complexity.

### J. Selection of parameters

We use the GPC metric to optimize the regularization parameters of all the algorithms, thus eliminating subjective biases in the choice of the parameters. In i-STORM experiments, the optimal parameters determined for one dataset work well for other datasets acquired in the same setting. The filter size parameter  $\sigma$  was initialized by  $10^{-4}$  and was

decreased by a factor of  $10^{-1}$  in each outer iteration. This continuation strategy helped provide fast convergence and minimize the oversmoothing resulted from averaging multiple neighbors. Our results show that 3-4 iterations are sufficient to get the best recovery. Adding more iterations did not further improve the weight matrix, and hence the reconstruction. We set the patch sizes in the proposed scheme to  $12 \times 12$  with a step size of 4 to ensure the patches are overlapped for better recovery. Smaller neighborhood and step sizes did not significantly improve the performance, while they resulted in slower reconstructions. Our experiments show that the above choice provided the best tradeoff between the computational complexity and the quality of reconstructions. The algorithm is terminated when the relative change in the cost function falls below small value  $\epsilon$ ; we have set  $\epsilon$  to  $10^{-6}$  in our scheme. The thresholding parameter,  $T$  was set to be about a half of the image maximum intensity value and divided by a small fraction in each outer iteration. The thresholding parameter  $T$  in (11) and regularization factor  $\lambda$  in both (8,12) were set to  $10^{-2}$  and  $10^{-6}$  respectively. We have kept the default value of PSF subspace dimension to 32.

## III. RESULTS

We compare our results with prior STORM and low-rank based partially separable functions (PSF) method [26] and temporal total variation & wavelet regularization scheme using Berkeley Advanced Reconstruction Toolbox (BART) [27].

Figure 2 shows the experiments on the simulated CINE dataset. We compare the navigator-free schemes i-STORM with patches and TV + Wavelet against navigator-based methods STORM and PSF. The simulated dynamic dataset is retrospectively undersampled using radial sampling pattern with 12 spokes, 4 navigator lines and 8 golden angle spokes per frame. The tables at the bottom of the figure show a quantitative comparison of the entire methods using SER, HFEN, SSIM and GPC metrics computed for the entire times series on both global FOV as well as a square region of interest containing the heart as shown in (f1).

In Figure 3, we compare the patch-based i-STORM against both i-STORM without patches and TV + Wavelet regularization. The navigator spokes were not used for estimating the manifold structure in both i-STORM versions. We also compare the results against STORM and PSF, both of which rely on navigators to estimate the manifold structure and subspace, respectively. All of the above methods rely on data from 300 frames ( $\approx 14$  seconds of acquisition) and is compared with the STORM reconstructions from 1000 frames whose acquisition time is  $\approx 50$  seconds. We report the GPC indices for the entire field of view (top value) and for a small region of interest containing the heart (bottom value) in the last column. We observe that the proposed i-STORM scheme (first row) provides less noisy and sharp reconstructions and is comparable in image quality to the STORM reconstructions from 1000 frames (bottom row). We show similar comparisons on another dataset in Figure 4 on both calibrated-based and calibrated-free acquisitions. The above prospective experiments show that the proposed patched-based i-STORM can facilitate a factor of three reductions in scan-time with minor loss in image quality.

#### IV. DISCUSSION AND CONCLUSION

We introduced a novel regularization approach to exploit the manifold structure of local image patches to recover dynamic MRI data from highly undersampled measurements. The proposed scheme could be seen as a generalized version of SToRM scheme, which exploits the global manifold structure of images in the dataset. The manifold structure of the patches are simpler and vary depending on the spatial location, hence this approach reduces the data demand and facilitates the recovery from shorter scans. Since the direct extension of SToRM to a patch setting is not possible, we relied on a regularization term that involves the sum of robust distances between images sub-patches in the dataset. We used a minimization scheme that alternates between the estimation of the manifold Laplacian and the recovery of the patches; this approach generalizes SToRM and eliminates the need for navigators to estimate the Laplacian. The new framework facilitates the reduction in the scan time by a factor of three, compared to the SToRM strategy.

The experiments on simulated datasets in Figure 2 shows that that i-SToRM provides reconstructions with lower spatial and temporal blurring, compared to other algorithms. While the quality of SToRM reconstruction is quite comparable to the proposed scheme, PSF and TV + Wavelet reconstructions exhibit motion artifacts and temporal blurring respectively. The residual images show that the errors associated with i-SToRM and SToRM are more homogeneously distributed in the entire image, thus providing reduced edge blurring and better preservation of fine features, including papillary muscles. By contrast, the errors with TV + Wavelet and PSF are more concentrated in the edge regions and around the myocardial wall, indicating edge blurring. The quantitative comparisons of the algorithms on this setting are shown in the bottom tables where we quantified the reconstruction by the signal-to-error ratio (SER), High Frequency Error (HFEN), Structural SIMilarity index (SSIM) and Global Phase Coherence (GPC) metrics computed for the whole time series on the entire FOV as well as a square region of interest containing the heart as shown in (f1). The quantitative metrics show about 1-4 dB SER improvement using i-SToRM compared to other reconstructions. The improvement behavior is consistent using HFEN, SSIM and GPC quantitative metrics.

In Figure 3, we observe that the i-SToRM with patches is almost comparable in performance to SToRM, which shows that the Laplacian can be estimated without the use of explicit navigators. This approach also facilitates the extension of SToRM to the patch setting. The main difference of i-SToRM scheme with SToRM is the iterative approach for the estimation of the manifold Laplacian, which eliminates the need for navigators. Also, we observe that i-SToRM without patches results in lower quality, indicating the need for local manifold modeling, especially when the Laplacian is estimated from the images themselves. We thus introduced patch-based i-SToRM, which provides a significant reduction in alias artifacts compared to the i-SToRM version without patches, thanks to exploiting the local manifold structure, compared to i-SToRM without patches. We also observe that

the performance of both PSF and TV + Wavelet schemes is worse than the SToRM schemes, especially in terms of the temporal profile and the noise amplification. This can be explained by the improved modeling of data by the non-linear manifold model, as opposed to the subspace model used in PSF or combination of sparse TV and Wavelet. As expected the SToRM with 300 frames result in increased noise, compared to the SToRM reconstructions shown in the bottom row, where the reconstruction relied on 1000 frames ( $\approx 50$  seconds of acquisition). By contrast, the patch-based i-SToRM shown in the second row is comparable in performance to the SToRM reconstructions with 1000 frames shown in the bottom row. Since SToRM and i-SToRM without patches rely on the similarity between images in the dataset, a large number of images are needed to ensure that all the phases are well represented. Hence, these methods require relatively long acquisition duration to ensure that the image manifold is well-sampled. By contrast, local patch manifolds are relatively simpler; fewer images (and hence shorter acquisitions) are sufficient to ensure good sampling of the corresponding patch manifolds. This translates to improved performance over TV + Wavelet and PSF. We considered the entire dataset recovery using SToRM prior in the bottom row for the sake of comparison.

The results in Figure 4 show the ability of the proposed i-SToRM scheme in recovering quality images comparable to SToRM without relying on navigator signals. Comparing the time profiles of the i-SToRM scheme between the navigated and non-navigated setting, we observe that the time profiles are smoother in the calibration-free dataset. This can be explained by the improved incoherence of sampling offered by the golden angle sequence. Note that the navigated sequence resulted in a 40% loss in efficiency due to the need for navigators. We can also see both TV + Wavelet and PSF exhibit considerable temporal motion artifacts or blurring. While i-SToRM is compared against SToRM and PSF using the calibration-based dataset, the calibrated-free dataset is recovered using only the proposed scheme as well as TV + Wavelet since both SToRM & PSF cannot estimate the manifold structure without navigators.

Our results demonstrate that using the local manifold structure of the image patches is superior to global manifold recovery. This approach is related to PRICE prior introduced in [17]. The main difference is the neighborhood to which each patch is compared. Specifically, PRICE compares each patch with its immediate neighbors, facilitating implicit motion-compensated reconstruction. Since this comparison has to be repeated for all the patches in the 3-D dataset, the computational complexity of the extension of PRICE scheme to this setting is challenging; it had been previously demonstrated on breath-held CINE and myocardial perfusion MRI applications, where the undersampling factor was considerably lower, when recovery from fewer image frames was sufficient. The number of inter-patch comparisons in the proposed scheme is lower by an order of magnitude. Specifically, we only compare each patch with patches in all the frames at the same location, which keeps the computational complexity manageable. The proposed implicit motion-resolved reconstruction can be viewed as an alternative

to binning strategies, which exploits the repetitive respiratory and cardiac motion. The benefit of the proposed scheme is that it does not require sophisticated approaches to estimate the motion phases, and is applicable to non-periodic motion applications such as speech and imaging of the digestive tract, where phase information is difficult to obtain; see [14] for examples of an application of STORM framework to speech imaging.

The utility of the proposed scheme is demonstrated in the context of simulated human phantoms as well as prospective free-breathing and ungated cardiac CINE MRI imaging with multichannel acquisitions. Future efforts will be directed towards an extension of the proposed scheme to a 3D multi-slice multi-channel acquisition.

#### V. ACKNOWLEDGEMENT

The authors would like to thank the reviewers for their valuable comments that significantly improved the quality of the manuscript. They also thank the authors of BART Toolbox and Professor Liang's group for making their code [27] and dataset [26] accessible online.

#### REFERENCES

- [1] S. Coppo, D. Piccini, G. Bonanno, J. Chaptinel, G. Vincenti, H. Feliciano, R. B. Van Heeswijk, J. Schwitter, and M. Stuber, "Free-running 4d whole-heart self-navigated golden angle mri: Initial results," *Magn Res Med*, vol. 74, no. 5, pp. 1306–1316, 2015.
- [2] M. Usman, D. Atkinson, C. Kolbitsch, T. Schaeffter, and C. Prieto, "Manifold learning based ecg-free free-breathing cardiac cine mri," *J Magn Reson*, vol. 41, no. 6, pp. 1521–1527, 2015.
- [3] S. G. Lingala, Y. Hu, E. DiBella, and M. Jacob, "Accelerated dynamic MRI exploiting sparsity and low-rank structure: kt SLR," *IEEE Trans Med Imag*, vol. 30, no. 5, pp. 1042–1054, 2011.
- [4] S. G. Lingala and M. Jacob, "Blind compressed sensing with sparse dictionaries for accelerated dynamic MRI," pp. 5–8, 2013.
- [5] B. Zhao, J. P. Haldar, A. G. Christodoulou, and Z.-P. Liang, "Image reconstruction from highly undersampled-space data with joint partial separability and sparsity constraints," *IEEE Trans Med Imag*, vol. 31, no. 9, pp. 1809–1820, 2012.
- [6] J. P. Haldar and Z.-P. Liang, "Spatiotemporal imaging with partially separable functions: a matrix recovery approach," in *IEEE I S Biomed Imaging: From Nano to Macro, Rotterdam, Netherlands*, pp. 716–719, 2010.
- [7] J. Royuela-del Val, L. Cordero-Grande, F. Simmross-Wattenberg, M. Martin-Fernandez, and C. Alberola-Lopez, "Nonrigid groupwise registration for motion estimation and compensation in compressed sensing reconstruction of breath-hold cardiac cine MRI," *Magn Res Med*, 2015, in process.
- [8] S. Lingala, E. DiBella, and M. Jacob, "Deformation corrected compressed sensing (DC-CS): A novel framework for accelerated dynamic MRI," *IEEE Trans Med Imag*, vol. 34, no. 1, pp. 72–85, 2015.
- [9] M. S. Asif, L. Hamilton, M. Brummer, and J. Romberg, "Motion-adaptive spatio-temporal regularization for accelerated dynamic MRI," *Magn Res Med*, vol. 70, no. 3, pp. 800–812, 2013.
- [10] C. Gilliam and T. Blu, "Local all-pass filters for optical flow estimation," *Proc. IEEE Int. Conf. Acoust Speech Signal Process. (ICASSP), Brisbane, Australia*, pp. 1533–1537, 2011.
- [11] T. Brox, A. Bruhn, N. Papenberg, and J. Weickert, "High accuracy optical flow estimation based on a theory for warping," *Computer Vision-ECCV*, pp. 25–36, 2004.
- [12] L. Feng, L. Axel, H. Chandarana, K. T. Block, D. K. Sodickson, and R. Otazo, "Xd-grasp: Golden-angle radial mri with reconstruction of extra motion-state dimensions using compressed sensing," *Magn Res Med*, vol. 75, no. 2, pp. 775–788, 2016.
- [13] A. G. Christodoulou, H. Zhang, B. Zhao, T. K. Hitchens, C. Ho, and Z.-P. Liang, "High-resolution cardiovascular MRI by integrating parallel imaging with low-rank and sparse modeling," *IEEE Trans Biomed Eng*, vol. 60, no. 11, pp. 3083–3092, 2013.
- [14] S. Poddar and M. Jacob, "Dynamic mri using smoothness regularization on manifolds (storm)," *IEEE Trans Med Imag*, vol. 35, no. 4, pp. 1106–1115, 2016.
- [15] U. Nakarmi, Y. Wang, J. Lyu, D. Liang, and L. Ying, "A kernel-based low-rank (klr) model for low-dimensional manifold recovery in highly accelerated dynamic mri," *IEEE Transactions on Medical Imaging*, vol. PP, no. 99, pp. 1–1, 2017.
- [16] Z. Yang and M. Jacob, "Nonlocal regularization of inverse problems: a unified variational framework," *IEEE Trans Image Process*, vol. 22, no. 8, pp. 3192–3203, 2013.
- [17] Y. Q. Mohsin, S. G. Lingala, E. DiBella, and M. Jacob, "Accelerated dynamic mri using patch regularization for implicit motion compensation," *Magn Res Med*, 2016.
- [18] Y. Q. Mohsin, G. Ongie, and M. Jacob, "Iterative shrinkage algorithm for patch-smoothness regularized medical image recovery," *IEEE Trans Med Imag*, vol. 34, no. 12, pp. 2417–2428, 2015.
- [19] J. Trzasko and A. Manduca, "Highly Undersampled Magnetic Resonance Image Reconstruction via Homotopic  $\ell_{\{0\}}$ -Minimization," *IEEE Trans Med Imag*, vol. 28, no. 1, pp. 106–121, 2009.
- [20] D. Geman and C. Yang, "Nonlinear image recovery with half-quadratic regularization," *IEEE Trans Image Process*, vol. 4, no. 7, pp. 932–946, 1995.
- [21] B. Zhao, J. P. Haldar, and Z.-P. Liang, "Psf model-based reconstruction with sparsity constraint: Algorithm and application to real-time cardiac mri," in *Engineering in Medicine and Biology Society (EMBC), 2010 Annual International Conference of the IEEE*, pp. 3390–3393, IEEE, 2010.
- [22] S. Ravishankar and Y. Bresler, "MR image reconstruction from highly undersampled k-space data by dictionary learning," *IEEE Trans Med Imag*, vol. 30, no. 5, pp. 1028–1041, 2011.
- [23] Z. Wang, A. C. Bovik, H. R. Sheikh, and E. P. Simoncelli, "Image quality assessment: from error visibility to structural similarity," *IEEE Trans Image Process*, vol. 13, no. 4, pp. 600–612, 2004.
- [24] G. Blanchet, L. Moisan, and B. Rougé, "Measuring the global phase coherence of an image," in *Proc. Int. Conf. on Image Processing*, pp. 1176–1179, 2008.
- [25] D. O. Walsh, A. F. Gmitro, and M. W. Marcellin, "Adaptive reconstruction of phased array mr imagery," *Magnetic Resonance in Medicine: An Official Journal of the International Society for Magnetic Resonance in Medicine*, vol. 43, no. 5, pp. 682–690, 2000.
- [26] C. Brinegar, Y.-J. L. Wu, L. M. Foley, T. K. Hitchens, Q. Ye, C. Ho, and Z.-P. Liang, "Real-time cardiac mri without triggering, gating, or breath holding," in *Engineering in Medicine and Biology Society, 2008. EMBS 2008. 30th Annual International Conference of the IEEE*, pp. 3381–3384, IEEE, 2008.
- [27] M. Uecker, F. Ong, J. I. Tamir, D. Bahri, P. Virtue, J. Y. Cheng, T. Zhang, and M. Lustig, "Berkeley advanced reconstruction toolbox," in *Proc. Intl. Soc. Mag. Reson. Med*, vol. 23, p. 2486, 2015.

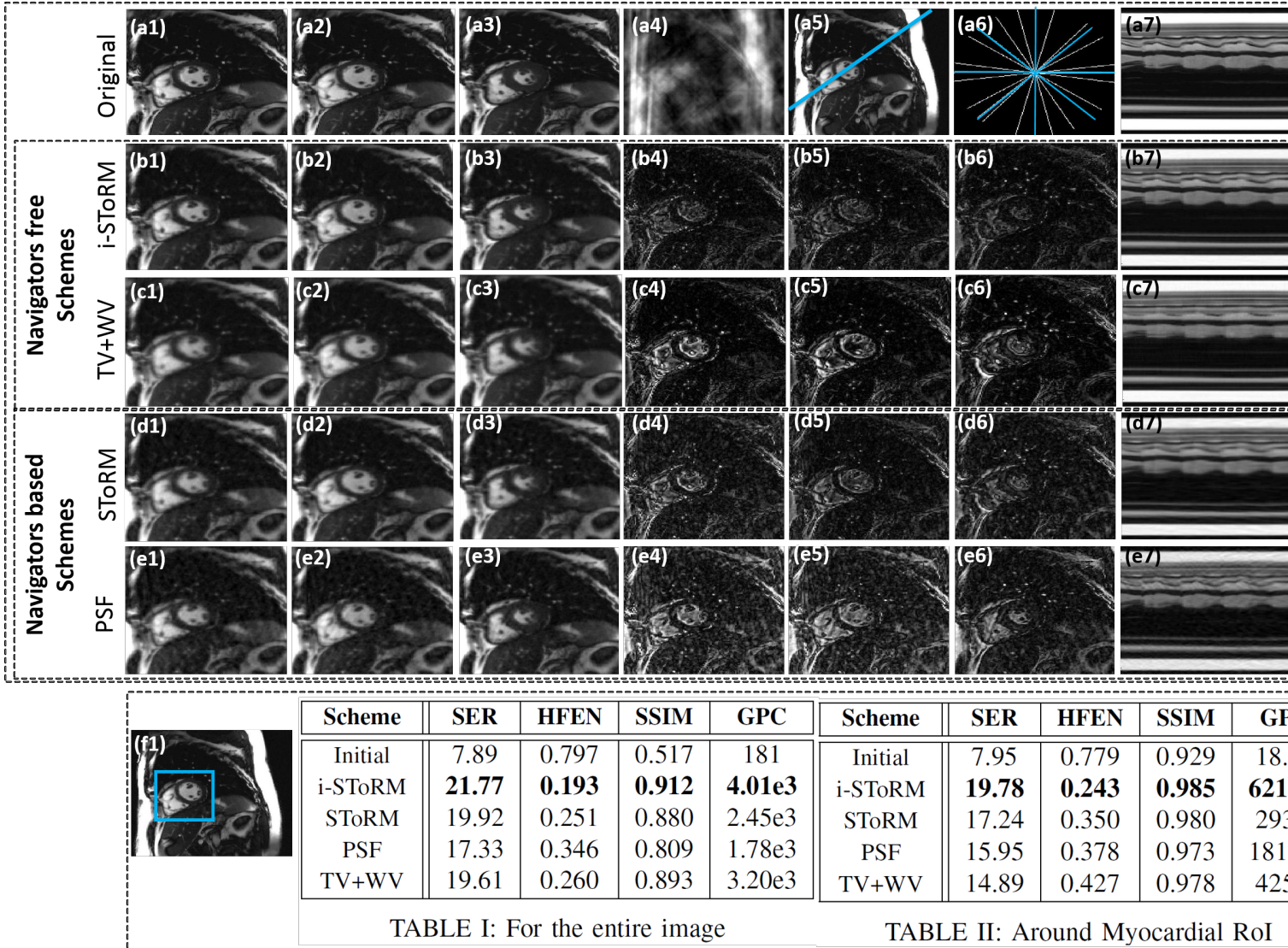


Fig. 2: Recovery of the simulated CINE dataset using patch-based i-SToRM (second row), TV + Wavelet (third row) calibration-based SToRM (fourth row) and calibration-based PSF scheme (last row). The simulated dynamic dataset in the top row is retrospectively undersampled using radial sampling pattern with 12 spokes, 4 navigator lines and 8 golden angle spokes per frame. Two frames of each reconstruction, corresponding to diastolic and systolic cardiac phases are shown. The images are cropped versions of the full frame shown in (a4), while (a3) is the initial guess. The error images are scaled by a factor of 5 for better visualization. The time profiles in the last column correspond to a line passing through the left ventricle and right ventricle shown in (a4). We observe that i-SToRM provides lower spatial and temporal blurring, compared to other algorithms. While SToRM reconstruction that uses navigators is comparable to the proposed scheme, PSF and TV + Wavelet reconstructions exhibit motion artifacts and temporal blurring respectively. The residual images show that the errors associated with i-SToRM and SToRM are more homogeneously distributed, indicating reduced edge blurring and better preservation of fine features, including papillary muscles. By contrast, the errors with TV + Wavelet and PSF are more concentrated in the edge regions and around the myocardial wall, indicating edge blurring. The table at the bottom of the figure show a quantitative comparison of the entire methods using SER, HFEN, SSIM and GPC metrics computed for the entire time series on both the whole field of view (left table) as well as around the region of interest (right table) shown in the blue box of sub-figure (f1).

		Mask					
		(a1)	(a2)	(a3)			
300 frames	Navigators free Schemes	Proposed i-Storm w patches	(b1)	(b2)	(b3)	(b4)	9.71e4 606.13
		i-Storm w/o patches	(c1)	(c2)	(c3)	(c4)	6.41e4 292.13
		TV + WV Scheme	(d1)	(d2)	(d3)	(d4)	3.2e4 210.5
		Navigators based Schemes	Storm Scheme	(e1)	(e2)	(e3)	(e4)
	PSF Scheme		(f1)	(f2)	(f3)	(f4)	2.5e4 113.82
	Storm Scheme		(g1)	(g2)	(g3)	(g4)	8.38e4 678

Fig. 3: Evaluation on a free breathing & ungated CINE dataset, acquired in the axial 4-chamber view. The dataset was acquired using the navigated acquisition scheme used in [14], which consists of 4 navigator lines and 6 golden angle spokes per frame. The sampling trajectory for one of the sampling patterns is shown in sub-figure (a1) with colored lines indicating the navigators that are the same for all frames. The time profiles in the fourth column are drawn for all of the recovered frames, along with the line passing through the cardiac region shown in (b1). The time instance of the specific frames are depicted in the time profiles with the color of their bounding boxes. Three frames of each reconstructed dataset are shown for demonstration. The images are zoomed versions around the square box shown in (a3) while (a2) is the initial guess. Subfigures (b1-b3), (c1-c3) and (d1-d3) show the recovery using navigator-free schemes: patch-based i-Storm, i-Storm without patches and TV + Wavelet respectively; while (e1-e3) and (f1-f2) show the recovery using navigator-based schemes STORM and PSF. The top five rows are recovered using only a subset of 300 frames, while the bottom row shows the data recovered from 1000 frames. STORM and PSF schemes, shown in the 5th - 7th rows, relied on navigators to estimate the global manifold Laplacian. The comparisons of the reconstructions from 300 frames show that the i-Storm scheme can provide comparable image quality to the STORM scheme, even though it did not rely on the navigators. This iterative approach enabled us to exploit the local manifold structure of the patches (i-Storm with patches), which significantly improved the performance over the global approach. The improved performance of STORM over PSF and TV + Wavelet methods, seen by a reduced blurring of image features and improved temporal profiles, can be attributed to the improved signal modeling offered by the non-linear manifold model compared to a subspace approach or sparsity regularization. Note that the image quality of the i-Storm with patches obtained from 300 frames is comparable to that obtained from STORM with 1000 frames. In the last column, we report the GPC indices for both the entire FOV, the top value, as well as around a small region of interest containing the heart shown in the bottom. The quantitative metric shows that the reconstruction of the proposed method using 300 frames are comparable to that 1000 dataset recovered using STORM.

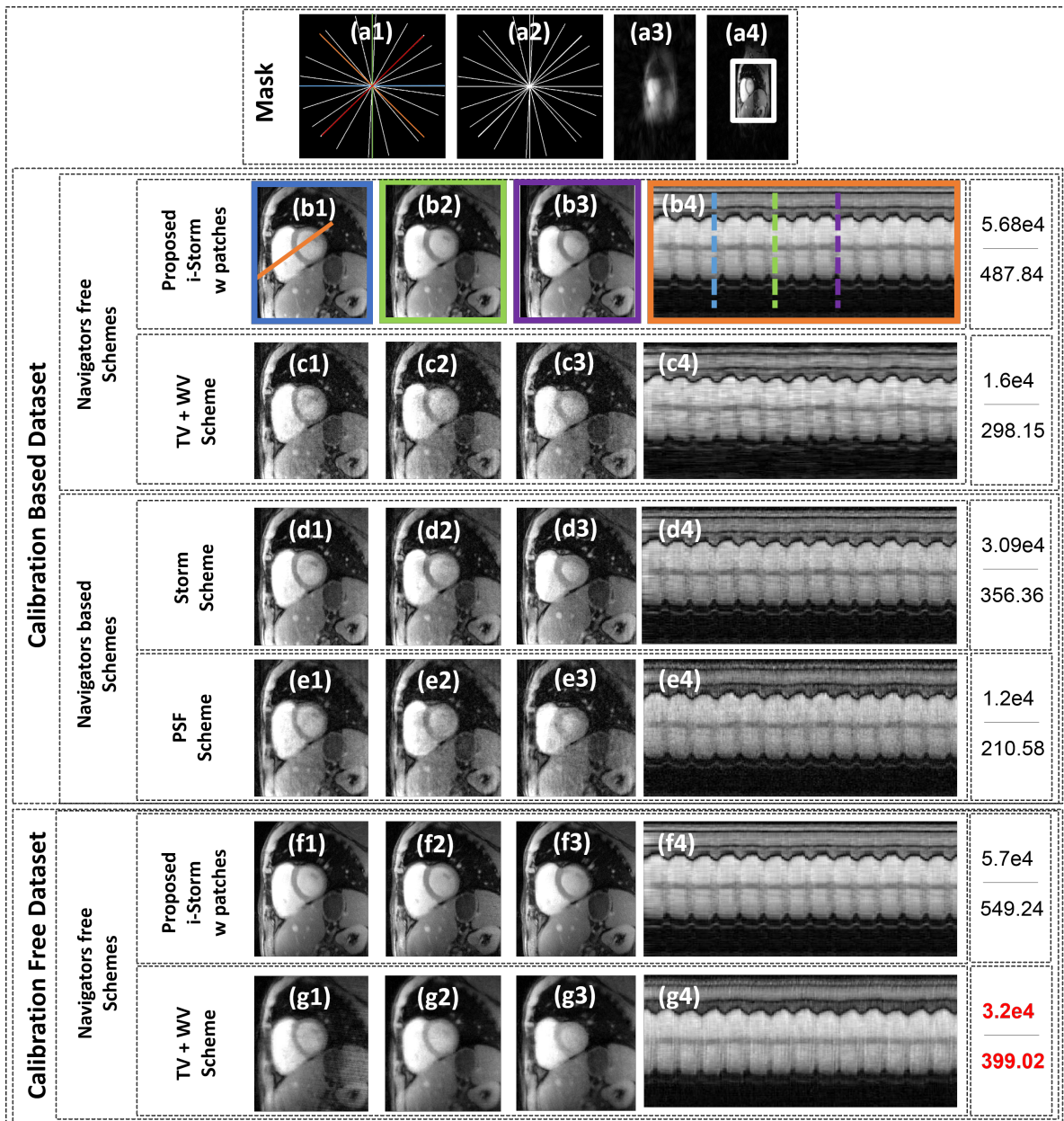


Fig. 4: Comparison of the algorithms on a free-breathing and ungated dataset in the short axis view. The dataset was collected with two acquisition schemes: a navigated acquisition scheme, as well as a golden angle sequence. The sampling trajectories for navigated and golden-angle schemes for one of the frames are shown in (a1) and (a2), respectively, where the colored lines indicating the fixed navigators that are the same for all frames. 300 frames of the time series (3000 spokes, which correspond to 14 seconds of acquisition) were considered for recovery. Note that there is no one-to-one correspondence between the calibrated and calibration-free acquisitions since they were acquired at two different time points, possibly with different respiratory patterns. (a3) is the initial guess, while (a4) is the corresponding frame recovered using patch-based i-SToRM. The zoomed versions of three frames, out of 300 frames, from different phases in the dataset are shown in the first three columns. The time profiles in the fourth column are drawn for all of the frames, along the line passing through the left ventricle and right ventricle as shown in (b1). i-SToRM is compared against SToRM and PSF using the calibration-based dataset, while the calibrated-free dataset is recovered using only the proposed scheme as well as TV + Wavelet; both SToRM & PSF cannot estimate the manifold structure without navigators. The results show the ability of the proposed i-SToRM scheme in recovering quality images comparable to SToRM without relying on navigator signals. Both TV + Wavelet and PSF exhibit considerable motion artifacts and temporal blurring. The last column shows the GPC indices for both the entire FOV, the top value, as well as around a small region of interest containing the myocardium shown in the bottom. The quantitative metric shows an improvement of the proposed method compared to other reconstructions.